Screened environment-dependent reactive empirical bond-order potential for atomistic simulations of carbon materials

Romain Perriot, Xiang Gu, You Lin, Vasily V. Zhakhovsky, and Ivan I. Oleynik
Department of Physics, University of South Florida, Tampa, Florida 33620, USA
(Received 23 March 2013; published 19 August 2013)

A screened environment-dependent reactive empirical bond-order (SED-REBO) potential has been developed for large-scale molecular dynamics (MD) simulations of carbon materials. Based on the second-generation REBO potential developed by Brenner and co-workers [J. Phys.: Condens. Matter **14**, 783 (2002)], the SED-REBO potential overcomes the deficiencies of the REBO potential, which arise from a short range of interatomic interactions and their abrupt switching off at the cutoff distance, by increasing the range of interatomic interactions and eliminating the explicit switching function while introducing a simple yet efficient screening function. The increased cutoff distance allows the inclusion of interactions critically important for the physically correct description of bond breaking and bond remaking. An analytic form of the attractive and repulsive pairwise terms was devised to automatically become zero at distances above the cutoff, thus, eliminating the need for the switching function. The screening function effectively screens off the second- and further-nearest-neighbor interactions for calculation of energy and forces in a smooth and continuous way for both compression and expansion. The pairwise attractive and repulsive terms were refitted within a wide range of interatomic distances to properly describe large compressions and expansions of diamond and graphene as well as their behavior near equilibrium. Good performances of the SED-REBO potential to describe bond-breaking processes at extreme tensile stresses are demonstrated in large-scale MD simulations of the nanoindentation of graphene membranes. A computationally efficient version of the SED-REBO potential is introduced for large-scale MD simulations of shock-wave compression in carbon materials. The SED-REBO potential is implemented as a module in the Large-Scale Atomic/Molecular Massively Parallel Simulator (LAMMPS) and is freely available.

DOI: 10.1103/PhysRevB.88.064101 PACS number(s): 61.50.Lt, 81.05.U−, 34.20.Cf, 82.20.Wt

I. INTRODUCTION

Elemental carbon, due to its ability to possess several hybridization states, exists in various allotropes including diamond, graphite, graphene, amorphous carbon, fullerenes, and carbon nanotubes (CNTs). The diversity of the unique physical and chemical properties of carbon materials is explored by atomistic simulations, which delivers information sometimes difficult or even impossible to obtain in experiments. For example, molecular dynamics (MD) simulations were used to investigate the fundamental growth mechanisms of the chemical vapor deposition of diamond;[1] properties of amorphous carbon films;[2–6] the friction, fracture, and indentation response of diamond and other carbon materials;[7–15] mechanical properties of carbon nanotubes,[16–23] graphene membranes, and nanoribbons;[24–32] formation of nanodiamonds under pressure;[33] carbon sputtering;[34] collision of carbon clusters;[35,36] and shock compression of diamond,[37,38] just to mention a few.

Interatomic potentials are at the heart of atomistic simulations; their ability to capture the essential physics and chemistry is of critical importance for the reliable prediction of fundamental materials properties. One of the popular carbon potentials is the reactive empirical bond-order (REBO) potential, originally developed by Brenner in 1990[39] and later improved by Brenner and co-workers in its second-generation version.[40] The REBO potential was extended by Stuart *et al.* to include torsional contributions for hindered rotations about single bonds and long-range dispersive interactions in the adaptive intermolecular REBO (AIREBO) potential.[41] The other notable carbon potentials are the environment-dependent interatomic potential (EDIP),[42] the long-range bond-order potential (LCBOP),[43–45] and the reactive force field (ReaxFF) potential.[46]

Most existing carbon potentials were developed with a focus on the behavior of carbon materials under normal conditions of ambient pressure and temperature. However, there is no guarantee that they perform well under conditions of high stresses and temperatures, which involve processes of bond making and bond remaking. Sometimes the existing interatomic potentials are used in simulations involving bond-breaking events without proper validation. For example, AIREBO and ReaxFF potentials are popular methods for studying the mechanical properties of graphene in regimes involving large stresses. Although ReaxFF performs much better than AIREBO, which mirrors the unsatisfactory behavior of the REBO potential as discussed below, both the AIREBO and the ReaxFF potentials fail to provide a quantitative description of bond-breaking phenomena in carbon materials (see the Supplemental Material).[47]

One illustrative example, involving the application of REBO-type interatomic potentials beyond their domain of applicability, is an erroneous prediction of ductile fracture in CNT[17,48] and graphene[49] under tensile stress, which is due to artificial strengthening of the bonds upon tensile deformations. These excessively large restoring forces arise from the switching function, which is used in the potentials to switch off the atomic interactions at a fixed cutoff distance r_c. The latter is usually chosen between the first- and the second-nearest-neighbor distances in uncompressed materials so that only nearest-neighbor interactions are included in calculations at normal conditions. Although the switching function does not influence interactions in materials under normal conditions,

it subjects atoms to large switching-induced forces under high tensile deformations because the interatomic distances fall within the switching region close to r_c. This causes the erroneous description of bond-breaking processes.

To correctly simulate the failure of a material at tensile loads, an interatomic potential should provide a good description of its spinodal instability, which occurs at a point where the bulk modulus becomes zero.[50] This critical "spinodal" bond length r^* is defined as an inflection point of the binding-energy curve $E(r)$, $d^2E(r^*)/dr^2 = 0$. Moreover, to deliver a physically viable mechanism of crack generation and propagation, the range of interatomic interactions should be extended beyond the point of mechanical instability at r^* to include explicit contributions of the interatomic interactions at distances larger than the lengths of the broken bonds.[51]

Several attempts were undertaken to improve the description of bond-breaking and bond-remaking phenomena within the REBO approach by increasing the fixed cutoff distance.[48,52,53] However, such simple analytic continuation of the original energy and force dependencies to distances $r > r_c$ does not guarantee good accuracy upon bond breaking because such distances were not included in the fitting database of the original REBO potential. More importantly, the increase in r_c results in contributions of second- and further-nearest-neighbor interactions, which contradicts the concept of the saturated covalent bond implemented in the angular-dependent REBO. The further-nearest-neighbor interactions also start to contribute at large compressions to energy and forces in the REBO potential with the original cutoff distance of $r_c = 2.0$ Å, producing an unphysically abrupt increase in energy upon compression.[54]

The contradiction between the requirements of having a first-nearest-neighbor model and a large cutoff can be constructively resolved by invoking the idea of effective screening of further-nearest-neighbor interactions. The interactions are discriminated by looking at the local environment about a bond, the screening function effectively playing the role of a variable cutoff. The fixed cutoff distance is set to be large enough to include unscreened nearest-neighbor interactions at large distances, covering the range critically important for bond-breaking phenomena. At the same time, the second- and further-nearest-neighbor interactions are effectively screened and, consequently, are removed from calculations of energy and forces at both normal conditions and under compression.

Baskes[55–57] was the first to develop the idea of screening while devising the modified embedded atom potential for metals (MEAM). This screening was also developed within the environment-dependent tight-binding model.[58–60] Screening was implemented in a MEAM-type potential for Si[61] as well as in two recent REBO-based carbon potentials.[49,62] However, both carbon REBO-type potentials still employ a switching function that produces artificially large forces within the switching regions.

This paper successfully addresses the fundamental difficulties arising from the short range of interatomic interactions and their abrupt switching off at the cutoff distance by introducing a new screened environment-dependent reactive bond-order (SED-REBO) potential, which was specifically developed to simulate carbon materials at extreme compressive and tensile stresses. By increasing the range of interatomic interactions, eliminating the explicit switching function, and introducing a simple yet efficient screening function, the SED-REBO potential provides for the first time the accurate description of bond-breaking and bond-remaking events in carbon systems under extreme tensile and compressive stresses. The excellent performance of the SED-REBO potential in describing bond breaking is illustrated in large-scale MD simulations of the nanoindentation of graphene membranes. A computationally efficient version of the SED-REBO potential has been developed for large-scale simulations of shock-compressed carbon materials.

II. DEVELOPMENT OF THE SED-REBO POTENTIAL

The new SED-REBO interatomic potential includes several critical advances. First, the cutoff distance r_c is increased beyond spinodal bond length r^* to $r_c = 3.3$ Å to include interatomic distances occurring in bond-breaking events at high tensile stresses. Second, it employs the screening function, which plays the role of a "variable cutoff" to maintain the first-nearest-neighbor nature of the potential. Third, the switching function is completely eliminated by using a new analytic form of pairwise repulsive and attractive functions with built-in switching behavior at r_c, thus, providing a smooth continuous dependence of the energy and forces on atomic coordinates in the entire region of interatomic distances $0 \leqslant r \leqslant r_c$. Fourth, the pairwise attractive and repulsive functions are refitted using density functional theory (DFT) binding-energy curves for graphene and diamond to cover small and large interatomic distances, which were previously excluded from the fitting database. Finally, computationally inexpensive but quite flexible analytic rational functions were employed to fit pairwise attractive and repulsive terms.

The general form of the SED-REBO potential is similar to the original REBO potential, except that the switching function $f_c(r_{ij})$ is replaced by an environment-dependent screening function S_{ij},

$$U = \frac{1}{2}\sum_{j\neq i} S_{ij}[V_R(r_{ij}) + b_{ij}V_A(r_{ij})], \tag{1}$$

where V_A and V_R are the attractive and repulsive pairwise functions and b_{ij} is the bond-order term.

The screening function S_{ij} for a bond i-j depends on the local environment surrounding the bond in the following way. A bond between two atoms i and j is not screened if there are no atoms in the neighborhood of the bond, $S_{ij} = 1$. If an atom k comes close to the i-j bond, its strength gradually decreases as new bonds are formed between pairs of atoms i-k and/or j-k. In the limiting case of an atom k positioned between i and j, the i-j bond is completely screened, $S_{ij} = 0$. This qualitative behavior is quantitatively accounted for by the analytic S_{ij} function, defined below in Eq. (2). As an illustration, S_{ij} is calculated for a bond i-j as a function of position of the neighboring atom k along the perpendicular line passing through the middle of the i-j bond, see Fig. 1. When the i-k distance is small (atomic configuration on the left in Fig. 1), atom k screens the i-j bond. As the i-k distance increases, the influence of atom k on the i-j bond diminishes

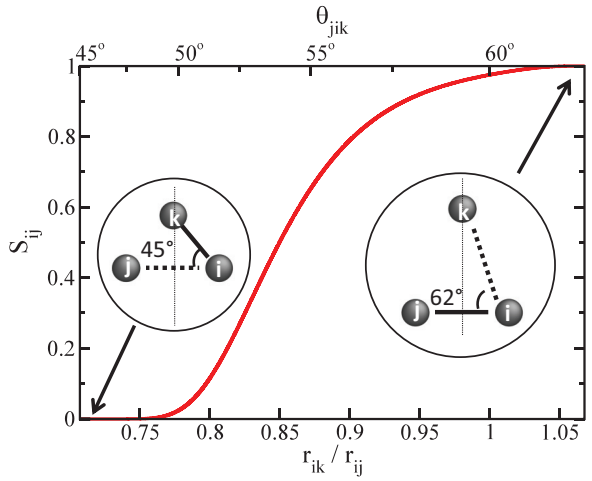

FIG. 1. (Color online) Screening function S_{ij} for a bond i-j as a function of the distance $r_{ik} = r_{jk}$ between the atom i (or j) and a neighbor atom k. The bond length r_{ij} is kept constant, whereas, atom k moves up along the perpendicular line passing through the midpoint of the bond. The left configuration displays screened bond i-j ($S_{ij} = 0$) and new bond i-k, and the right configuration—unscreened bond i-j ($S_{ij} = 1$) and no bond between atoms i and k.

(S_{ij} increases). Finally, the i-j becomes unscreened ($S_{ij} = 1$), see the atomic configuration on the right in Fig. 1.

The screening function S_{ij} for bond i-j depends on the bond length r_{ij} and the environment (env(i-j)) around the bond,

$$S_{ij}(r_{ij},\mathrm{env}(i\text{-}j)) = \exp\left(-\sum_{k\neq i,j}(g_{ijk})^n\right), \qquad (2)$$

where k is a neighbor of atoms i and j. The individual contribution g_{ijk} due to atom k is calculated as

$$g_{ijk} = \begin{cases} \dfrac{r_{ij}}{\bar{R}_{ik}+\bar{R}_{jk}-r_{ij}} - \frac{1}{2}, & \bar{R}_{ik}+\bar{R}_{jk} \leqslant 3r_{ij}, \\ 0, & \bar{R}_{ik}+\bar{R}_{jk} > 3r_{ij}, \end{cases} \qquad (3)$$

with

$$\bar{R}_{ik(jk)} = \bar{R}(r_{ik(jk)}) \equiv \frac{r_{ik(jk)}}{1-(r_{ik(jk)}/r_c)^m}. \qquad (4)$$

The condition $\bar{R}_{ik}+\bar{R}_{jk} \leqslant 3r_{ij}$ in Eq. (3) defines an ellipsoid around the i-j bond, which contains possible positions of neighboring atoms k contributing to the screening of the i-j bond.

The functional form of the screening function S_{ij} is adapted from Ref. 61 with an important modification: renormalized interatomic distances $\bar{R}_{ik}, \bar{R}_{jk}$, rather than interatomic distances r_{ik}, r_{jk}, are used in Eq. (3). They are introduced to ensure the continuity of the potential energy, defined in Eq. (1), when a neighboring atom is approaching the interaction region defined by the cutoff distance r_c. To illustrate the situation, a simple case of the symmetric configuration $r_{ik} = r_{jk}$ is displayed in Fig. 2(a) where only an upper half of the entire picture above the i-j bond is shown for simplicity. The semi-ellipse with the red boundary specifies the region $r_{ik}+r_{jk} \leqslant 3r_{ij}$ where $g_{ijk} \neq 0$, and the dashed and dotted semicircles represent the boundaries of the interaction regions $r_{ik(jk)} \leqslant r_c$ for neighbors of atom $i(j)$.

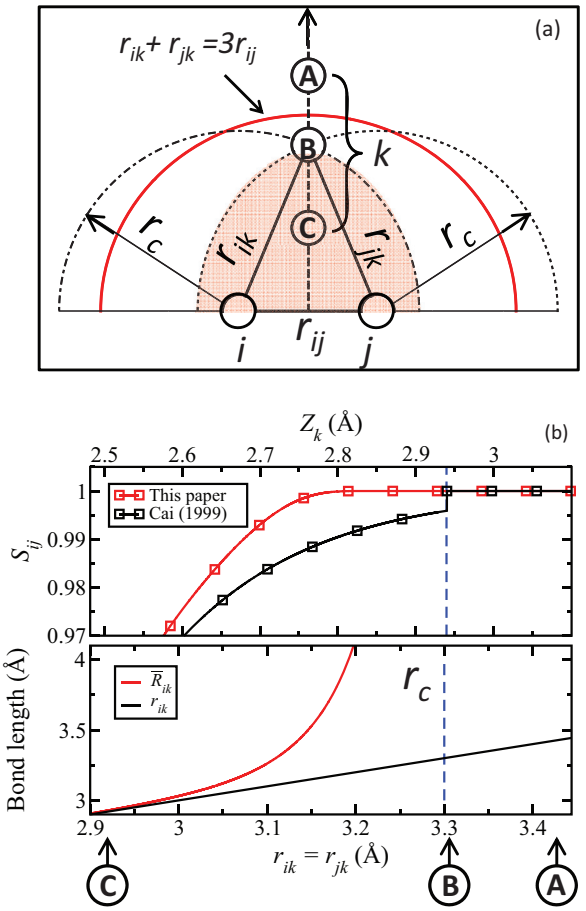

FIG. 2. (Color online) Effect of the renormalized distance $\bar{R}$, Eq. (4), on the screening function S_{ij} for the case of a neighboring atom k approaching the fixed bond i-j (with $r_{ij} = 3.0$ Å) along the line perpendicular to the bond, $r_{ik} = r_{jk}$. Panel (a) displays the geometry where only the upper half of the entire picture above the i-j bond is shown for simplicity. The semi-ellipse with the red boundary specifies the region $r_{ik}+r_{jk} \leqslant 3r_{ij}$ where $g_{ijk} \neq 0$, see Eq. (3); dashed and dotted semicircles represent the boundaries of the interaction regions $r_{ik(jk)} \leqslant r_c$ for a neighbor k of atom $i(j)$. The intersection of all three regions is indicated by a pink segment referred to as a screening region. Panel (b) shows the dependence of two screening functions S_{ij} on the distance $r_{ik} = r_{jk}$: the original S_{ij} from Ref. 61, which uses $r_{ik} = r_{jk}$—black line, and the S_{ij} used in this paper, which employs renormalized distances $R_{ik} = R_{jk}$—red line. The original S_{ij} from Ref. 61 displays discontinuity from $S_{ij} = 1$ to $S_{ij} \neq 1$ when atom k crosses the boundary of the screening region while moving from above towards the i-j bond. The lower panel of (b) shows the dependence of the renormalized distance $\bar{R}_{ik}$ on distance r_{ik}. $\bar{R}_{ik}$ approaches infinity at the cutoff distance $r_{ik} = r_c$, thus, avoiding a discontinuity in S_{ij}.

An atom k contributes to S_{ij} if it belongs to the intersection of all three regions, which is referred to as a screening region shown in Fig. 2(a) as a pink segment. When an atom k crosses the boundary of the screening region while moving from above towards the i-j bond, the original screening function S_{ij} from Ref. 61 experiences a jump from $S_{ij} = 1$ to $S_{ij} \neq 1$, which causes a discontinuity in energy and forces, see Fig. 2(b). To solve this problem, renormalized distances $\bar{R}_{ik}, \bar{R}_{jk}$ are introduced, see Eq. (4). The renormalized distance

is constructed to have $R_{ik} = \infty$ when atom k enters the interaction region $r_{ik} \leqslant r_c$ of atom i. This ensures that $S_{ij} = 1$ when atom k crosses the boundary of the screening region with a subsequent decrease in S_{ij} as atom k approaches the i-j bond. Figure 2(b) shows S_{ij} as a function of the bond length $r_{ik} = r_{jk}$ for the case with $r_{ij} = 3.0$, $r_c = 3.3$ Å, and $n = 5$. The S_{ij} calculated using renormalized distances $\bar{R}_{ik}, \bar{R}_{jk}$ displays a continuous behavior in contrast to S_{ij} calculated using r_{ik} and r_{jk}.

An attractive feature of the screening function S_{ij} is its dependence on the ratio of the atomic distances rather than their absolute values, allowing effective screening in systems having the same topology of first-, second-, and further-nearest neighbors at both compressions and expansions of the system.

The adjustable parameters n and m in Eqs. (2) and (4) determine the strength of the screening and the divergence rate of renormalized distances, respectively. Several combinations of values for n and m were screened in the graphene membrane "pull-out" computational experiment, see Sec. III D. It was found that switching behavior is quite insensitive to specific values of these parameters. Therefore, the values $n = 5$ and $m = 48$ were chosen to achieve the best agreement between DFT and SED-REBO data.

The bond-order function b_{ij} in Eq. (1) is defined as in Ref. 40, except that the switching function $f_c(r_{ij})$ is replaced by the product $f_c \times S_{ij}$ such that the screening discriminates between first- and further-nearest neighbors,

$$b_{ij} = \frac{1}{2}\left(b_{ij}^{\sigma-\pi} + b_{ji}^{\sigma-\pi}\right) + b_{ij}^{\pi}, \tag{5}$$

$$b_{ij}^{\sigma-\pi} = \left[1 + \sum_{k\neq i,j} f_c(r_{ik}) \times S_{ik}(r_{ik},\mathrm{env}(i\text{-}k)) \times G(\cos(\theta_{ijk}))e^{\lambda_{ijk}} + P_{ij}\left(N_i^C, N_i^H\right)\right], \tag{6}$$

$$b_{ij}^{\pi} = \pi_{ij}^{RC} + b_{ij}^{DH}. \tag{7}$$

The switching function $f_c(r_{ik})$ is still needed inside the bond order b_{ij} because the screening function $S_{ik}(r_{ik},\mathrm{env}(i\text{-}k))$ depends on ratios but not on absolute values of the interatomic distances; see Eqs. (2) and (3). Therefore, $S_{ik}(r_{ik},\mathrm{env}(i\text{-}k))$ cannot be used alone to describe a continuous change in the coordination number of atom i as its neighbor k enters the interaction sphere $r_{ik} \leqslant r_c$ and starts contributing to the bond-order term $b_{ij}^{\sigma-\pi}$. The product $f_c(r_{ik}) \times S_{ik}(r_{ik},\mathrm{env}(i\text{-}k))$ gives a smooth change from 0 to some nonzero value as atom k enters the interaction sphere $r_{ik} \leqslant r_c$ and excludes any contributions to b_{ij} from the fully screened bond i-k.

The expressions for the quantities λ_{ijk}, N_i^C, N_i^H, the spline function P_{ij}, the angular term $G(\cos(\theta))$, as well as the conjugation π^{RC} and dihedral b_{ij}^{DH} contributions are given in the original second-generation REBO potential paper.[40] All of these terms were kept the same as in Ref. 40, except for the switching function $f_c(r_{ik})$, which was replaced by the product $f_c(r_{ik}) \times S_{ik}(r_{ik},\mathrm{env}(i\text{-}k))$. Modifications of the bond-order term b_{ij} were specifically avoided to preserve all of the essential physics and chemistry of chemical bonding incorporated in the original REBO potential. Rather, the current paper concentrates on the accurate description of bond-breaking and bond-remaking processes under large tensile and compressive stresses, which are not properly described by REBO.

The switching function f_c, used in the bond-order term, takes a different form compared to that in the original REBO,

$$f_c(r) = \begin{cases} 1, & r < r_{\min}, \\ 1 - \chi^3\left(6\chi^2 - 15\chi - 10\right), & r_{\min} \leqslant r \leqslant r_{\max}, \\ 0, & r > r_{\max}, \end{cases} \qquad \chi = (r - r_{\min})/(r_{\max} - r_{\min}). \tag{8}$$

The polynomial form of f_c is similar to that used in Ref. 41. It has an advantage over the cosine function used in the original REBO potential: both $f_c(r)$ and its first and second derivatives are continuous at the boundaries $r = r_{\min}$ and $r = r_{\max}$ for the interval of interatomic distances where the switching function is applied. Therefore, the energy, forces, and their first derivatives are continuous functions of atomic coordinates, which results in a better conservation of energy during numerical integration of Newton's equations of motion. The values for the parameters $r_{\min}$ and $r_{\max}$ are 3.0 and 3.3 Å, respectively.

Finally, the pairwise repulsive V_R and attractive V_A terms are expressed as analytical rational functions,

$$V(r) = \frac{\bar{r}^3}{r^{A_1}} \times \frac{A_2 + A_3\bar{r} + A_4\bar{r}^2 + A_5\bar{r}^3 + A_6\bar{r}^4}{1 + B_3\bar{r} + B_4\bar{r}^2 + B_5\bar{r}^3 + B_6\bar{r}^4}, \tag{9}$$

where $\bar{r} = r - r_c$. By using $\bar{r}$ instead of r, the pairwise functions and their first and second derivatives are automatically zero at the cutoff distance r_c. Therefore, the switching function is not required. Thus, the artificial forces present in the REBO potential due to switching functions are not observed in the SED-REBO potential; see Figs. 3 and 4 in which REBO, SED-REBO, and DFT energies, along with their first derivatives, are compared for the cases of diamond and graphene upon isotropic compressions and expansions.

The pairwise attractive V_A and repulsive V_R terms in the SED-REBO expression, Eq. (1), were fitted to graphene and diamond DFT binding-energy curves in the range of interatomic distances of 0.5 Å $\leqslant r \leqslant$ 2.7 Å. The isotropic compressions and expansions do not change the topology of the ideal crystal lattice. Therefore, the bond-order term is constant, the screening function is $S_{ij} = 1$ for first-nearest neighbors and is zero for all other further-nearest neighbors. These simplifications allow the extraction of numerical values of the V_R and V_A at each interatomic distance, which then were fitted using analytic rational function representation, Eq. (9). The excellent quality of the fit is evident from Figs. 3 and 4, which compare SED-REBO binding energies and the forces along the C-C bond with DFT and old REBO data. The parameters of the SED-REBO potential can be found in the Supplemental Material.[63]

III. SED-REBO VALIDATION

A. Graphene and diamond properties

An important test of the new SED-REBO potential is concerned with the mechanical properties of graphene and diamond (see Table I), which include elastic constants C_{ij}, bulk modulus B_0 and its pressure derivative B_0' for diamond, two-dimensional (2D) elastic modulus E^{2D} for graphene,

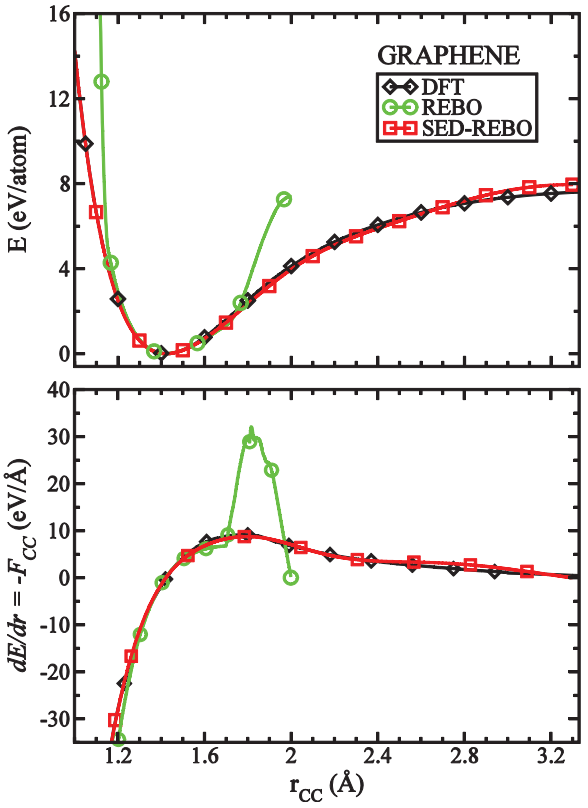

FIG. 3. (Color online) Binding energy E and its first derivative dE/dr upon isotropic compression and expansion of graphene as a function of nearest-neighbor distance r_{CC}: comparison between REBO, SED-REBO, and DFT. Large artificial forces appear within the switching region of 1.7 Å $\leqslant r \leqslant$ 2.0 Å of the REBO potential, whereas, the SED-REBO potential has a nice smooth behavior throughout the entire range of interatomic distances in excellent agreement with DFT.

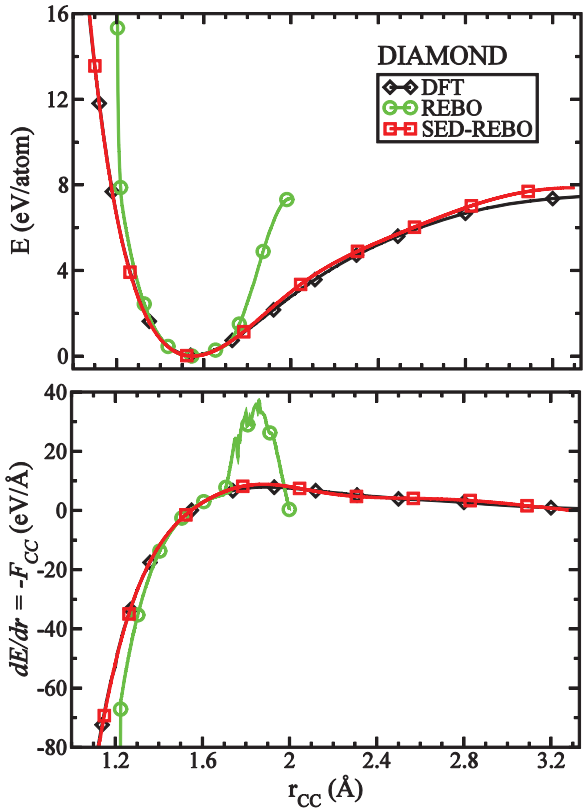

FIG. 4. (Color online) Binding energy E and its first derivative dE/dr upon isotropic compression and expansion of diamond as a function of nearest-neighbor distance r_{CC}: comparison between REBO, SED-REBO, and DFT. Large artificial forces appear within the switching region of 1.7 Å $\leqslant r \leqslant$ 2.0 Å of the REBO potential, whereas, the SED-REBO potential has a nice smooth behavior throughout the entire range of interatomic distances in excellent agreement with DFT.

and diamond's $\sigma^*_\diamond$ and graphene's σ^*_{gr} breaking strengths. Although the graphene and diamond binding-energy curves were included in the fitting of the SED-REBO potential, their first derivatives (interatomic forces and stresses) and second derivatives (elastic constants) were not. In contrast, the elastic constants were included in the REBO fitting database.[40] As seen from Figs. 3 and 4, the graphene and diamond interatomic forces between a pair of carbon atoms are in very good agreement with the DFT data over a wide range of interatomic distances.

For the purpose of consistent comparison, the REBO and DFT elastic properties were recalculated to address some errors and inconsistencies in previous papers. For example, Brenner *et al.*[40] reported $C_{12} = 100$ GPa and $C_{44} = 680$ GPa for diamond, whereas, Stuart *et al.*[41] obtained $C_{12} = 120$ GPa and $C_{44} = 720$ GPa, citing discussions with Brenner and co-workers. The bulk modulus was obtained from the Birch-Murnaghan fit of pressure versus volume $P(V)$ upon hydrostatic compressions-expansions. The elastic constants were calculated by fitting stress-strain curves upon 2% compression-expansion of the lattice along specific crystallographic directions.

As seen from Table I, the SED-REBO bulk modulus B_0 for diamond and elastic constant C_{11} for both graphene and diamond are in good agreement with both REBO and DFT data, even though the SED-REBO C_{11} and B_0 were not fitted as was done in the case of REBO. An error of $\sim$30% in C_{12}, obtained by the SED-REBO potential, is not surprising as an error of the same magnitude was seen for REBO's C_{44}, which was not included in the fitting database either. These errors in C_{12} and C_{44} can easily be addressed in future work by including the uniaxial compressions and expansions in the fitting database. The SED-REBO elastic modulus E^{2D} of graphene obtained from the stress-strain curve upon equibiaxial expansion is in good agreement with both DFT and REBO. The experimental value of E^{2D} was not measured directly but was obtained from nanoindentation experiments. Therefore, a 10% experimental error can be attributed to the existence of complicated three-dimensional (3D) deformations, which were analyzed by the finite-element method to extract the value of E^{2D}; see Ref. 64.

The breaking strengths of graphene σ_{gr} and diamond $\sigma_\diamond$ are important indicators of the quality of the bond-breaking description by the new potential. They are obtained as spinodal maxima of 2D pressure σ for graphene and 3D pressure P for diamond upon isotropic expansion/compression of the lattice; see Fig. 5. As discussed above, the REBO potential fails to correctly predict the breaking strengths of

TABLE I. Mechanical properties of graphene and diamond: comparison of SED-REBO results with REBO, DFT, and experimental data.

		SED-REBO	REBO[a]	DFT[b]	Expt.
Graphene	r_0 (Å)	1.422	1.420	1.425	1.421[c]
	C_{11} (N/m)	337.7	352.4	351.5	370.4[d]
	C_{12} (N/m)	47.8	49.1	59.9	46.4[d]
	E^{2D} (N/m)	380.2	387.0	373.0	340[e]
	σ^*_{gr} (N/m)	30.4	102.0	32.2	42[e]
Diamond	r_0 (Å)	1.549	1.544	1.547	1.545[c]
	C_{11} (GPa)	1096.3	1053.1	1086.0	1076[f]
	C_{12} (GPa)	88.8	137.8	129.7	125[f]
	C_{44} (GPa)	736.5	711.8	585.5	576[f]
	B_0 (GPa)	424.6	442.9	448.5	442[f]
	B'_0	3.0	4.7	3.9	4.0[g]
	$\sigma^*_\diamond$ (GPa)	90.0	360.0	80.2	

[a]Recalculated in this paper.
[b]Calculated in this paper.
[c]From Ref. 65.
[d]From Ref. 66 using 3.34 Å as the thickness of graphene for conversion from GPa to N/m.
[e]From Ref. 64.
[f]From Ref. 67.
[g]From Ref. 68.

graphene and diamond due to excessively high maxima in forces produced by the REBO switching function in the cutoff region ($\sigma^*_\diamond = 360$ GPa). In contrast, the SED-REBO potential provides the values of $\sigma^*_{gr} = 30.4$ N/m and $\sigma^*_\diamond = 90.0$ GPa in good agreement with DFT: $\sigma^*_{gr} = 32.2$ N/m and $\sigma^*_\diamond = 80.2$ GPa. The experimental breaking strength of diamond under isotropic expansion is unknown. In the case of graphene, the experimental σ^*_{gr} was obtained indirectly from nanoindentation experiments with the use of finite-element analysis,[64] which explains the somewhat higher value of the experimental σ^*_{gr} compared to those obtained from DFT and SED-REBO calculations.

B. Binding-energy curves and structural stability

As is well known, graphite is the lowest-energy crystal structure of carbon, metastable diamond being slightly higher in energy. Both REBO and SED-REBO correctly describe the relative stability of graphene (one layer of graphite) compared to diamond. Other zero-dimensional (0D), one-dimensional (1D), and three-dimensional (3D) structures of carbon, such as dimer, linear chain (LC), simple cubic (SC), face-centered cubic (FCC), and body-centered cubic (BCC) are much higher in energy, which makes their experimental observation highly unlikely. Nevertheless, we calculated the binding-energy curves with the SED-REBO potential and determined the relative structural stability as judged by the corresponding energies per atom at the minimum of the binding-energy curves. The energy scale was set to zero at the minimum of the diamond binding-energy curve; see Fig. 6. In addition, equilibrium lattice parameters for these structures that correspond to minima of the binding-energy curves were also obtained.

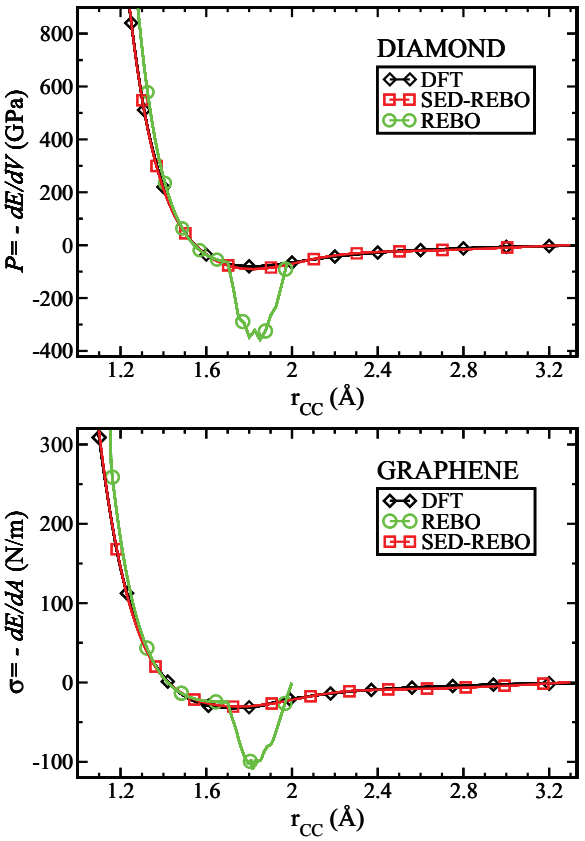

FIG. 5. (Color online) Three-dimensional pressure for diamond P and two-dimensional pressure for graphene σ. The breaking strength σ^* of a material is defined as the pressure at the spinodal point $\partial P/\partial V = 0$.

In Table II, the SED-REBO structural stability predictions and equilibrium properties are compared with those obtained from REBO and DFT calculations. The structural ordering, graphene → diamond → LC → SC → BCC → FCC, is predicted by SED-REBO in agreement with DFT; see Fig. 6

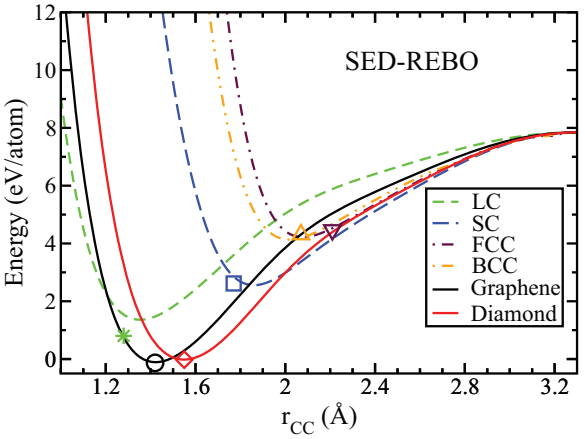

FIG. 6. (Color online) SED-REBO binding-energy curves for 1D linear chain, 2D graphene, and 3D simple cubic, face-centered cubic, and body-centered cubic, and diamond crystal structures of carbon. Similarly colored symbols indicate positions of the corresponding minima obtained from DFT calculations.

TABLE II. Equilibrium bond length and energies for various carbon structures calculated using SED-REBO, REBO, and DFT. The binding energy of diamond at the minimum of the binding-energy curve is taken as the reference energy.

	SED-REBO		REBO		DFT[a]	
	E_0 (eV)	r_0 (Å)	E_0 (eV)	r_0 (A)	E_0 (eV)	r_0 (Å)
Dimer	4.580	1.349	4.265	1.325	4.238	1.243
LC	1.380	1.353	1.253	1.332	0.823	1.27
Graphene	−0.091	1.422	−0.025	1.420	−0.111	1.42
Diamond	0.000	1.549	0.000	1.544	0.000	1.55
SC	2.576	1.860			2.637	1.77
BCC	4.154	2.019			4.331	2.07
FCC	4.241	2.079			4.486	2.21

[a]Calculated in this paper.

and Table II. This is quite remarkable as only graphene and diamond binding-energy curves were included in the fitting database. In addition, the SED-REBO binding energies at the minima are close to the DFT energies. In contrast, the REBO potential fails to produce minima in binding-energy curves for SC, FCC, and BCC structures because their minima are either in the switching region (SC) or outside the cutoff region (FCC and BCC). Physically correct structural predictions by the SED-REBO potential are a sign of its markedly improved transferability compared to the REBO potential.

C. Graphene nanoribbon pull-out experiment

To investigate the performance of the SED-REBO potential in simulating bond-breaking phenomena in carbon systems, a simple but physically illuminating model is used: a single atom pulled out of a graphene nanoribbon (GNR) edge. The system consists of a rectangular piece of graphene (30 Å × 14 Å), periodically repeated in the lateral direction. The relatively small size of the system allows us to perform DFT calculations to validate SED-REBO predictions. A zigzag row of the atoms at the bottom of the sample is pinned while a central atom at the top zigzag edge is pulled up vertically in increments of 0.05 Å, all the atoms being constrained to be in the vertical plane of the GNR, see the inset in Fig. 7. After each displacement of the central atom, the entire system is relaxed using the conjugate gradient (CG) algorithm while keeping the bottom zigzag row and the top central atom fixed.

The energy of the system as a function of the atom displacement, obtained using REBO, SED-REBO, and DFT, is shown in Fig. 7. The SED-REBO and REBO predictions of the GNR response to the pull-out of the central atom are noticeably different: the REBO energy exhibits unphysically high jumps upon height increase of the central atom, whereas, the SED-REBO energy follows the DFT energy, which does not have such large jumps. A careful examination of the evolution of the GNR geometry, simulated by the REBO potential, shown in Fig. 8, reveals the formation of a chain of atoms out of the GNR edge. As the central atom moves up, the energy increases until the next atom from the GNR is extracted from the bulk. The formation of the new bond within the chain is accompanied by a substantial drop in energy.

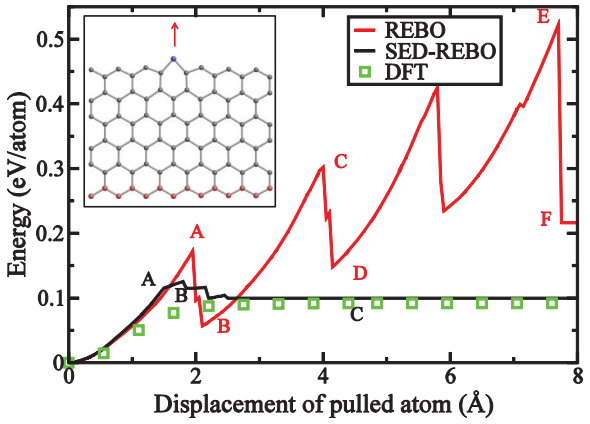

FIG. 7. (Color online) Graphene nanoribbon pull-out experiment: energy of the system as a function of the vertical displacement of the central atom. The red-colored atoms are at the fixed bottom edge, and the blue-colored atom is the atom being pulled up. The periodic boundary condition is applied in the lateral direction. Letters A–F label special events displayed in Figs. 8 and 9.

The appearance of chains in MD simulations of fracture in carbon materials is a characteristic feature of the REBO bond-breaking processes.[17,49] This artifact of the REBO potential is entirely due to the application of the switching function to turn off the interactions at the cutoff distance r_c. As seen in Fig. 3, a pair of atoms experiences a substantial increase in mutually attractive forces, resulting in artificial strengthening of the C-C bond for large interatomic distances within the switching region. At the end of the process, the chain of carbon atoms is formed out of the GNR edge, whereas, the sample exhibits a substantial remnant plasticity; see Fig. 8. In particular, large unbroken hexagons are formed within the graphene lattice as seen in snapshots (d) and (e) of Fig. 8.

The chain formation, obtained using the REBO potential, is in contradiction with DFT simulations, which demonstrate a monotonic decrease in mutual attraction as the two atoms are pulled apart. Both the increase in the cutoff distance from $r_c = 2.0$ to $r_c = 3.3$ Å and the complete elimination of the switching function in the SED-REBO potential solve this critical deficiency of the REBO potential and provide

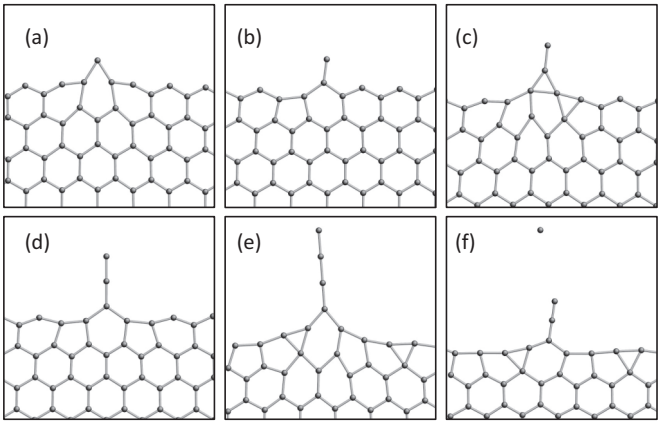

FIG. 8. Evolution of the graphene nanoribbon atomic structure during the pull-out experiment obtained by the REBO potential. Snapshots (a)–(f) correspond to events A–F in Fig. 7.

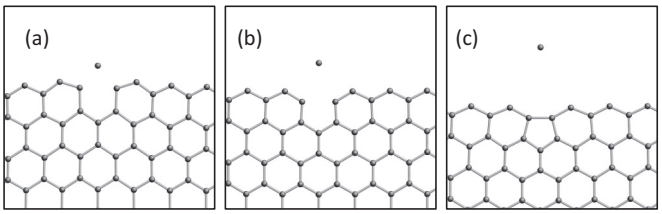

FIG. 9. Evolution of the graphene nanoribbon atomic structure during the pull-out experiment obtained by the SED-REBO potential. Snapshots (a)–(c) correspond to events A–C in Fig. 7.

a physically viable mechanism of bond breaking in close agreement with DFT. Instead of chain formation, the two bonds between the pulled atom and its first neighbors break, followed by a relaxation of the free boundary of graphene containing a single vacancy defect; see Fig. 9.

D. Graphene membrane "pull-down" experiment

This computational test was designed to simulate the bond-breaking phenomenon that occurs during the indentation of a circular graphene membrane by a pointlike indenter. The zigzag edge of the membrane is fixed, and the central carbon atom of the membrane is pulled down in a succession of incremental indentation depths δ. At each δ, all the atoms, other than the central atom, are relaxed using the conjugate gradient algorithm; see Fig. 10. The relatively small size of the system ($\sim$10 Å in diameter) makes it possible to perform DFT calculations, thus, allowing a direct comparison of SED-REBO and REBO results with first-principles data.

The REBO potential produces a markedly different picture of membrane indentation compared to both DFT and the SED-REBO potential: the energy per atom versus indentation depth δ curve, shown in Fig. 11, displays an increase in the energy before the membrane breaks five times larger (0.6 eV/atom) than that predicted by both the SED-REBO potential and the DFT (0.12 eV/atom). This enormous energy increase is the

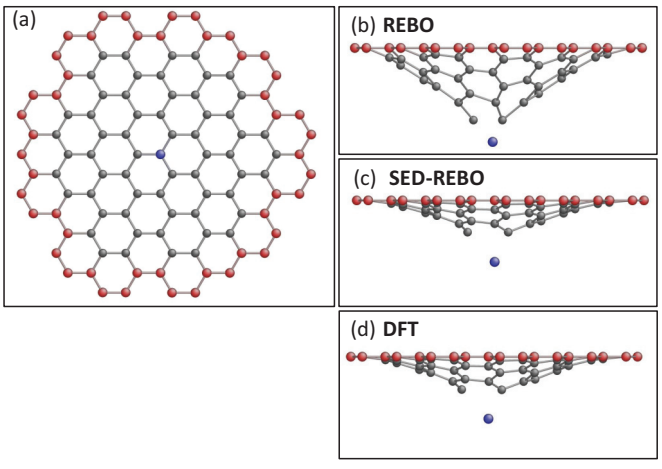

FIG. 10. (Color online) Graphene membrane pull-down computational experiment. (a) Top view of the system in the initial state. Red-colored atoms are in the fixed edge of the membrane, and the central blue-colored atom is the atom being pulled down. (b)–(d) Side views of the membrane at the moment before failure obtained by REBO, SED-REBO, and DFT, respectively.

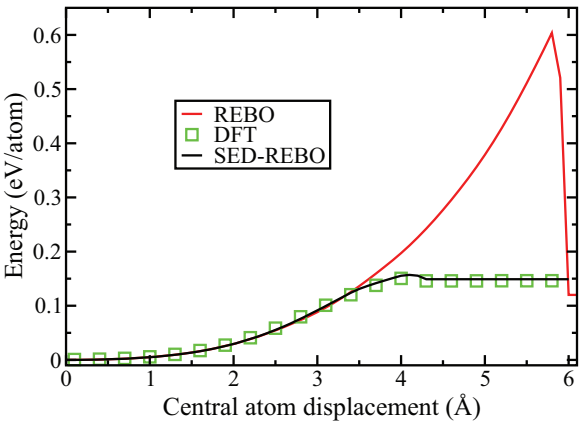

FIG. 11. (Color online) Energy of the system as a function of the vertical displacement of the central atom during the pull-down computational experiment performed using REBO, SED-REBO, and DFT.

consequence of the strengthening of the C-C bonds upon the increase in bond lengths in the cutoff region; see discussion above. As the central atom is pulled down, the artificially large forces in the cutoff region pull its first neighbors, they, in turn, pull their neighbors, etc. In fact, due to the collective effect of the strengthening of the C-C bonds in the cutoff region, the pulling down of the central atom causes a large number of atoms in the central region of the membrane to respond; see Fig. 10(b).

In contrast, the SED-REBO potential displays a behavior which closely resembles that of DFT. As the central atom is pulled down, the bond lengths to its first-nearest neighbors increase as the corresponding forces decrease until a critical bond-breaking length is reached, resulting in the failure of the membrane. The further-nearest-neighbor atoms located away from the central atom are affected insignificantly; see Fig. 10(c) for a picture of the membrane's geometry right before the failure. The DFT calculations produce almost identical results; see Figs. 10(d) and 11. As mentioned in Sec. II, parameters n [strength of screening, Eq. (2)] and m [rate of divergence of the renormalized distance, Eq. (4)] of the screening function were checked to produce good agreement with DFT in the graphene pull-down experiment. It was found that the specific values of parameters n and m hardly affect the results, which is not surprising. The role of the screening is to select first-nearest-neighbor interactions and to discard all the further neighbors, which is not so sensitive to the values of n and m. The actual behavior upon bond breaking is defined by the dependence of energy and forces upon distance in the vicinity of the spinodal point, which was carefully fitted during the SED-REBO potential development, see Sec. II.

IV. APPLICATION TO NANOINDENTATION OF GRAPHENE MEMBRANES

Two previous small-scale pull-out and pull-down tests revealed markedly different behaviors of the REBO and SED-REBO potentials: the REBO potential displaying plastic deformations characteristic of a ductile response to the tensile load and the SED-REBO potential displaying a brittle

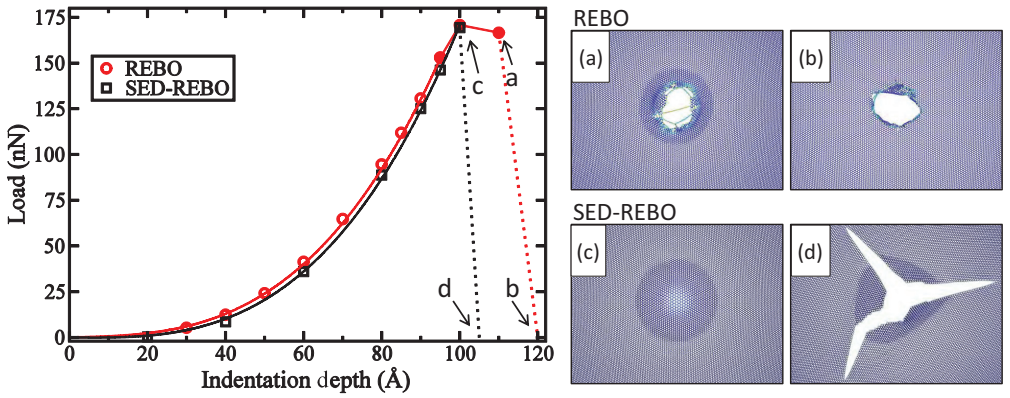

FIG. 12. (Color online) Left panel: REBO and SED-REBO indentation curves (load versus indentation depth) obtained from the nanoindentation of a circular graphene membrane with a diameter of $D = 800$ Å by a spherical indenter with a radius of $R = 30$ Å. Solid symbols represent the first instance of defect appearance. Right panels: central part of the membrane (about 120×100 Å^2). Panels (a) and (b) display the atomic structure obtained using the REBO potential at indentation depths of 110 and 120 Å, respectively. Panels (c) and (d) display atomic structure obtained using the SED-REBO potential at indentation depths of $\delta = 100$ and 105 Å, respectively.

fracture initiated by a single bond-breaking event. The ductile behavior of the REBO potential, observed during large-scale MD simulations of the nanoindentation of circular graphene membranes,[69,70] was the major motivation to address its failures by developing the SED-REBO potential.

MD simulations of graphene nanoindentation were performed to investigate, in detail, the performance of the new SED-REBO potential in real situations. The graphene sample was a 800 Å diameter circular membrane (∼200 000 atoms), the outer edge being fixed. The indenter was represented by a spherical repulsive potential of a radius of 30 Å. For a given indentation depth, the initial shape of the membrane was prepared by imposing the profile of the membrane under a point load obtained analytically from nonlinear elasticity theory.[71] Then, the system was relaxed using the CG algorithm. To activate possible bond-breaking events, the membrane was subjected to elevated temperatures up to 1000 K and, then, was cooled down to 0 K, followed by the final CG relaxation step. Finally, the load was determined by calculating the force exerted by the spherical tip.

The indentation curve, load F versus indentation depth δ, calculated by both REBO and SED-REBO, is shown in Fig. 12. Both potentials display similar behavior at moderate indentation depths in agreement with experiment:[64] F increases linearly with δ at small indentation depths, then, $F \sim \delta^3$ at large δ. The differences between the REBO and the SED-REBO potentials appear at large indentation depths of $\delta > 100$ Å: the membrane simulated by REBO displays plastic deformations due to the appearance of defects resulting in a deviation from the δ^3 behavior. The defects consist of voids and long linear chains of carbon atoms as seen from point (a) in the left panel of Fig. 12 and the corresponding frame (a) in the right panel. These defects are very similar to those observed in previous MD simulations of CNT under a tensile load using the REBO potential.[17,49] Further increase in the load results in breaking of the carbon chains and the appearance of a hole roughly the size of the contact area with the indenter; see frame (b) in Fig. 12. The SED-REBO potential displays a very different failure mode: no defects appear until a critical load is reached as seen from point (c) in the left panel of Fig. 12, and the corresponding frame (c) in the right panel. Above the critical load, large cracks are opened up and propagate deeply into the membrane, causing a catastrophic failure, as seen in frame (d) in Fig. 12 in agreement with experiment.[64] The markedly different failure modes exhibited by the REBO and SED-REBO potentials were also observed during large-scale MD simulations of the dynamical indentation of membranes of large diameters.

V. SED-REBO POTENTIAL FOR SHOCK COMPRESSION OF DIAMOND

The environment-dependent screening is also important for a proper description of compressed carbon materials. As discussed earlier, the compression reduces first-, second-, and further-nearest-neighbor distances so that, within the fixed cutoff scheme employed within the REBO potential, these further-nearest-neighbor atoms start to contribute to the energy and forces, resulting in an unphysically large increase in total energy. In fact, the unphysically abrupt increase in the total energy upon uniaxial compression of diamond crystal along the ⟨110⟩ crystallographic direction at interatomic distances of $r_{cc} < 1.2$ Å results in the numerical overflow of the calculations for compressions $V/V_0 < 0.75$; see Fig. 13. The screening function employed in SED-REBO avoids the inclusion of further-nearest neighbors, thus, limiting contributions to first-nearest neighbors only. This key improvement is of critical importance for robust MD simulations of shock compression in diamond.

In principle, the SED-REBO potential presented above can be directly used in MD simulations of compressed carbon materials. However, due to SED-REBO's large cutoff of $r_c = 3.3$ Å, which was absolutely necessary to describe the bond-breaking processes in the case of the tensile loads, the MD simulation of compressed carbon materials would involve unnecessary calculations for further-nearest-neighbor interactions, which are eventually discarded because the corresponding screening functions are equal to zero. In contrast to REBO, which uses a fixed functional form of switching function, the switching off of the interatomic interactions

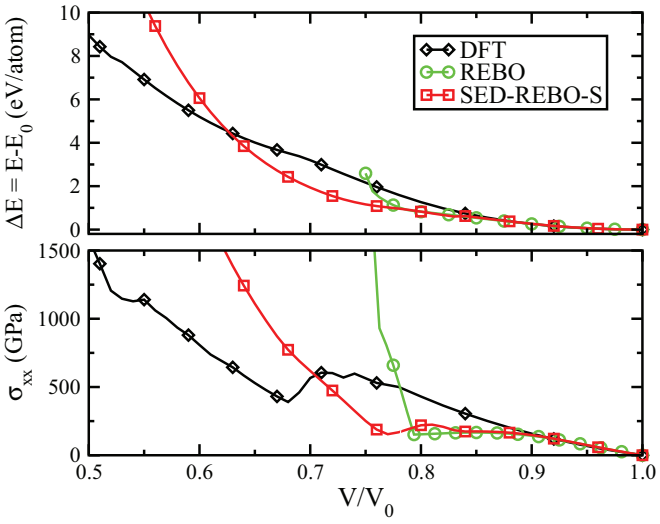

FIG. 13. (Color online) Uniaxial compression of diamond crystal along the ⟨110⟩ direction: relative energy (top panel) and longitudinal stress σ_{xx} (bottom panel) as a function of the compression ratio V/V_0.

is embedded in SED-REBO's pairwise repulsive V_R and attractive V_A functions. Because the cutoff radius r_c is a parameter of the pairwise functions [see Eq. (9)], its change requires refitting of the SED-REBO potential.

A version of the SED-REBO potential, referred to as SED-REBO-S, which utilizes a shorter cutoff of $r_c = 2.0$ Å, was specifically developed for MD simulations of compressed carbon materials. The same functional form for V_R and V_S as in Eq. (1) was used with the new cutoff of $r_c = 2.0$ Å. The SED-REBO-S binding-energy curve for diamond is almost indistinguishable from that calculated using either the SED-REBO potential or the DFT for interatomic distances $r_{CC} < 1.65$ Å; whereas, the REBO binding-energy curve displays a markedly different behavior including a vertical asymptote at $r_{CC} \approx 1.2$ Å; see Fig. 14. Although the binding energy dependence of SED-REBO-S deviates substantially from both SED-REBO and DFT at distances of $r_{CC} > 1.7$ Å, this is of no importance as these C-C nearest-neighbor distances are not encountered within the compressed material, whereas,

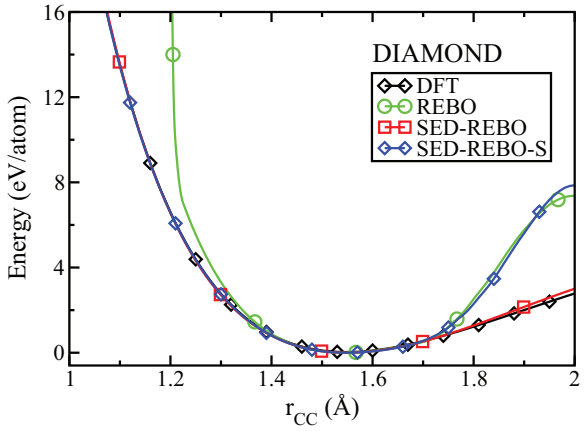

FIG. 14. (Color online) Diamond binding-energy curves obtained using REBO, SED-REBO, SED-REBO-S, and DFT.

all further-nearest neighbors are screened out and do not contribute to the energy and forces.

Because the diamond binding-energy curve was included in the SED-REBO-S fitting database, the potential describes diamond under large hydrostatic compressions well. However, the shock compression of diamond[72,73] involves uniaxial compressions. Therefore, the performance of the SED-REBO-S and REBO potentials upon uniaxial compression of diamond along the ⟨110⟩ crystallographic direction was evaluated and was compared with corresponding DFT data (see Fig. 13), which displays the energy and longitudinal stress dependence as a function of compression ratio. The behavior of the SED-REBO-S potential is substantially improved compared to that of the REBO potential. As seen from Fig. 13, the REBO energy and longitudinal stress σ_{xx} exhibit a sudden jump at a relatively moderate compression ratio of $V/V_0 \approx 0.8$ due to the appearance of second-nearest-neighbor atoms within the fixed cutoff distance of $r_c = 2.0$ Å. In contrast, the SED-REBO potential displays a much smoother response up to very high compressions.

Although the SED-REBO-S potential removes the unphysical behavior of the REBO potential at uniaxial compression, it exhibits some deviations from DFT at large uniaxial compressions; see Fig. 13. This is due to the fact that uniaxial compressions involve local atomic structures significantly different from those observed in uncompressed diamond and graphene, which were used in the fitting of the angular function of the bond-order term in Eq. (6) in Ref. 40, the latter being used without any substantial changes in this paper. The limited sampling of the bond angles during the fitting of the original REBO potential is a probable cause of deviations of both REBO and SED-REBO from DFT at large compressions. The improvement of the bond order to properly account for large uniaxial compressions is the subject of future work.

VI. CONCLUSIONS

A SED-REBO potential has been developed for large-scale simulations of carbon materials. By increasing the range of interatomic interactions, eliminating the explicit switching function, and introducing a simple yet efficient environment-dependent screening function, the SED-REBO potential resolves deficiencies of the REBO potential and provides an accurate description of bond-breaking and bond-remaking events in carbon systems under extreme tensile and compressive stresses.

The new SED-REBO potential provides a realistic description of bond-breaking events during the nanoindentation of graphene. In contrast to the REBO potential, which produces ductile behavior in contradiction to experiment, the SED-REBO potential correctly predicts brittle fracture, i.e., opening up and propagation of large cracks in the graphene membrane under an indenter load. The SED-REBO-S potential, a computationally efficient version of the SED-REBO potential, has also been developed for large-scale MD simulations of carbon materials at large compressions and is being used in large-scale MD simulations of shock-wave propagation in diamond. See preliminary results in Ref. 74.

Although the application of the environment-dependent screening function makes the SED-REBO potential superior

to the REBO potential in describing compressive and tensile states of carbon materials, it is of comparable quality as far as the properties of diamond and graphene near equilibrium are concerned. The SED-REBO potential uses a bond-order term practically identical to that of the REBO potential, but the attractive V_A and repulsive V_R pairwise terms were refitted in the current work. This was required due to the introduction of a novel analytic functional form of the attractive V_A and repulsive V_R pairwise terms as well as the need to cover a much wider range of interatomic distances corresponding to compressive and tensile states of the material. In principle, the quality of SED-REBO predictions can be substantially improved by extensive fitting of the bond-order term. However, the functional form of REBO, including the bond-order term, has some limitations, which are reflected in substantial deviations of REBO and SED-REBO predictions from DFT upon uniaxial compression; see Fig. 13. Therefore, future work on improving the SED-REBO potential will involve the systematic development of a robust analytic bond-order potential for carbon, which will combine the ideas of environment-dependent screening and the analytic bond-order potentials based on the tight-binding description of the electronic structure.[75–79]

The SED-REBO potential is implemented as a module in the Large-Scale Atomic/Molecular Massively Parallel Simulator (LAMMPS)[80] and is freely available.[81]

ACKNOWLEDGMENTS

This work was supported by NRL, ONR, and DTRA. Simulations were performed using the NSF XSEDE facilities, the USF Research Computing Cluster, and the computational facilities of the Materials Simulation Laboratory at USF. The authors thank C. T. White for enlightening discussions.

[1] B. J. Garrison, E. J. Dawnkaski, D. Srivastava, and D. W. Brenner, Science **255**, 835 (1992).
[2] N. Marks, Diamond Relat. Mater. **14**, 1223 (2005).
[3] H. U. Jäger and K. Albe, J. Appl. Phys. **88**, 1129 (2000).
[4] H. U. Jäger and A. Yu. Belov, Phys. Rev. B **68**, 024201 (2003).
[5] N. A. Marks, N. C. Cooper, D. R. McKenzie, D. G. McCulloch, P. Bath, and S. P. Russo, Phys. Rev. B **65**, 075411 (2002).
[6] L. M. Ghiringhelli, J. H. Los, E. J. Meijer, A. Fasolino, and D. Frenkel, Phys. Rev. B **69**, 100101(R) (2004).
[7] A. Garg and S. B. Sinnott, Phys. Rev. B **60**, 13786 (1999).
[8] G. T. Gao, P. T. Mikulski, and J. A. Harrison, J. Am. Chem. Soc. **124**, 7202 (2002).
[9] A. Garg, J. Han, and S. B. Sinnott, Phys. Rev. Lett. **81**, 2260 (1998).
[10] Y. Mo, K. T. Turner, and I. Szlufarska, Nature (London) **457**, 1116 (2009).
[11] M. Neek-Amal and F. M. Peeters, Phys. Rev. B **81**, 235421 (2010).
[12] G. Gao, R. J. Cannara, R. W. Carpick, and J. A. Harrison, Langmuir **23**, 5394 (2007).
[13] J. A. Harrison, C. T. White, R. J. Colton, and D. W. Brenner, Phys. Rev. B **46**, 9700 (1992).
[14] J. A. Harrison, C. T. White, R. J. Colton, and D. W. Brenner, Surf. Sci. **271**, 57 (1992).
[15] O. A. Shenderova, D. W. Brenner, A. Omeltchenko, X. Su, and L. H. Yang, Phys. Rev. B **61**, 3877 (2000).
[16] B. I. Yakobson, C. J. Brabec, and J. Berhnolc, Phys. Rev. Lett. **76**, 2511 (1996).
[17] B. Yakobson, M. Campbell, C. Brabec, and J. Bernholc, Comput. Mater. Sci. **8**, 341 (1997).
[18] V. Sazonova, Y. Yaish, H. Ustünel, D. Roundy, T. A. Arias, and P. L. McEuen, Nature (London) **431**, 284 (2004).
[19] K. M. Liew, C. H. Wong, X. Q. He, M. J. Tan, and S. A. Meguid, Phys. Rev. B **69**, 115429 (2004).
[20] S. L. Mielke, D. Troya, S. Zhang, J.-L. Li, S. Xiao, R. Car, R. S. Ruoff, G. C. Schatz, and T. Belytschko, Chem. Phys. Lett. **390**, 413 (2004).
[21] H. Zhao, K. Min, and N. R. Aluru, Nano Lett. **9**, 3012 (2009).
[22] S. Iijima, C. Brabec, A. Maiti, and J. Bernholc, J. Chem. Phys. **104**, 2089 (1996).
[23] J. Bernholc, D. Brenner, M. Buongiorno Nardelli, V. Meunier, and C. Roland, Annu. Rev. Mater. Res. **32**, 347 (2002).
[24] V. B. Shenoy, C. D. Reddy, A. Ramasubramaniam, and Y. W. Zhang, Phys. Rev. Lett. **101**, 245501 (2008).
[25] A. Fasolino, J. H. Los, and M. I. Katsnelson, Nat. Mater. **6**, 858 (2007).
[26] C. D. Reddy, S. Rajendran, and K. M. Liew, Nanotechnology **17**, 864 (2006).
[27] C. D. Reddy, A. Ramasubramaniam, V. B. Shenoy, and Y.-W. Zhang, Appl. Phys. Lett. **94**, 101904 (2009).
[28] F. Scarpa, S. Adhikari, and A. Srikantha Phani, Nanotechnology **20**, 065709 (2009).
[29] M. Neek-Amal and F. M. Peeters, Phys. Rev. B **82**, 085432 (2010).
[30] K. Min and N. R. Aluru, Appl. Phys. Lett. **98**, 013113 (2011).
[31] J. Hu, X. Ruan, and Y. P. Chen, Nano Lett. **9**, 2730 (2009).
[32] Q. Lu, M. Arroyo, and R. Huang, J. Phys. D **42**, 102002 (2009).
[33] N. Pineau, L. Soulard, J. H. Los, and A. Fasolino, J. Chem. Phys. **129**, 024708 (2008).
[34] J. Marian, L. A. Zepeda-Ruiz, G. H. Gilmer, E. M. Bringa, and T. Rognlien, Phys. Scr., **T124**, 65 (2006).
[35] R. C. Mowrey, D. W. Brenner, B. I. Dunlap, J. W. Mintmire, and C. T. White, J. Phys. Chem. **95**, 7138 (1991).
[36] Y. Yamaguchi and J. Gspann, Phys. Rev. B **66**, 155408 (2002).
[37] S. V. Zybin, M. L. Elert, and C. T. White, Phys. Rev. B **66**, 220102 (2002).
[38] S. V. Zybin, I. I. Oleynik, M. L. Elert, and C. T. White, *Synthesis, Characterization, and Properties of Energetic/Reactive Nanomaterials* (MRS, Warrendale, PA, 2003), p. 800:AA7.7.1.
[39] D. W. Brenner, Phys. Rev. B **42**, 9458 (1990).
[40] D. W. Brenner, O. A. Shenderova, J. A. Harrison, S. J. Stuart, B. Ni, and S. B. Sinnott, J. Phys.: Condens. Matter **14**, 783 (2002).
[41] S. J. Stuart, A. B. Tutein, and J. A. Harrison, J. Chem. Phys. **112**, 6472 (2000).
[42] N. A. Marks, Phys. Rev. B **63**, 035401 (2000).
[43] J. H. Los, L. M. Ghiringhelli, E. J. Meijer, and A. Fasolino, Phys. Rev. B **72**, 214102 (2005).
[44] L. M. Ghiringhelli, J. H. Los, A. Fasolino, and E. J. Meijer, Phys. Rev. B **72**, 214103 (2005).
[45] J. H. Los and A. Fasolino, Phys. Rev. B **68**, 024107 (2003).
[46] A. C. T. van Duin, S. Dasgupta, F. Lorant, and W. A. Goddard, J. Phys. Chem. A **105**, 9396 (2001).

[47]See Supplemental Material at http://link.aps.org/supplemental/10.1103/PhysRevB.88.064101 for a comparison of AIREBO, ReaxFF, and SED-REBO potentials with DFT in a series of validation tests involving compression and expansion of diamond and graphene as well as the pull-down experiment described in Sec. III D.
[48]B.-W. Jeong, J.-K. Lim, and S. B. Sinnott, Appl. Phys. Lett. **90**, 023102 (2007).
[49]L. Pastewka, P. Pou, R. Pérez, P. Gumbsch, and M. Moseler, Phys. Rev. B **78**, 161402(R) (2008).
[50]M. Born and K. Huang, *Dynamical Theory of Crystal Lattices* (Oxford University Press, New York, 1954).
[51]S. L. Mielke, T. Belytschko, and G. C. Schatz, Annu. Rev. Phys. Chem. **58**, 185 (2007).
[52]T. Belytschko, S. P. Xiao, G. C. Schatz, and R. S. Ruoff, Phys. Rev. B **65**, 235430 (2002).
[53]M. Sammalkorpi, A. Krasheninnikov, A. Kuronen, K. Nordlund, and K. Kaski, Phys. Rev. B **70**, 245416 (2004).
[54]I. I. Oleynik, A. C. Landerville, S. V. Zybin, M. L. Elert, and C. T. White, Phys. Rev. B **78**, 180101(R) (2008).
[55]M. I. Baskes, Phys. Rev. B **46**, 2727 (1992).
[56]M. I. Baskes, Mater. Sci. Eng. A **261**, 165 (1999).
[57]M. I. Baskes, Mater. Chem. Phys. **50**, 152 (1997).
[58]M. S. Tang, C. Z. Wang, C. T. Chan, and K. M. Ho, Phys. Rev. B **53**, 979 (1996).
[59]C. Z. Wang, B. C. Pan, and K. M. Ho, J. Phys.: Condens. Matter **11**, 2043 (1999).
[60]D. Nguyen-Manh, D. G. Pettifor, and V. Vitek, Phys. Rev. Lett. **85**, 4136 (2000).
[61]J. Cai, Phys. Status Solidi B **212**, 9 (1999).
[62]T. Kumagai, S. Hara, J. Choi, S. Izumi, and T. Kato, J. Appl. Phys. **105**, 064310 (2009).
[63]See Supplemental Material at http://link.aps.org/supplemental/10.1103/PhysRevB.88.064101 for parameters of the SED-REBO and SED-REBO-S potentials.
[64]C. Lee, X. Wei, J. W. Kysar, and J. Hone, Science **321**, 385 (2008).
[65]D. R. Lide, *CRC Handbook of Chemistry and Physics*, 90th ed. (CRC Press, Boca Raton, FL, 2009).
[66]A. Bosak, M. Krisch, M. Mohr, J. Maultzsch, and C. Thomsen, Phys. Rev. B **75**, 153408 (2007).
[67]C. Kittel, *Introduction to Solid State Physics*, 8th ed. (Wiley, Hoboken, NJ, 2005).
[68]H. J. McSkimin and J. P. Andreatch, J. Appl. Phys. **43**, 2944 (1972).
[69]R. Perriot, X. Gu, and I. I. Oleynik, in *Probing Mechanics at Nanoscale Dimensions*, edited by N. Taunura, A. Minor, C. Murray, and L. Friedman (MRS, Warrendale, PA, 2009), p. 1185:II05.04.
[70]R. Perriot, X. Gu, Y. Lin, V. V. Zhakhovsky, and I. I. Oleynik (to be published).
[71]S. Timoshenko, *Theory of Plates and Shells*, 2nd ed. (McGraw-Hill, New York, 1959).
[72]J. M. Lang and Y. M. Gupta, J. Appl. Phys. **107**, 113538 (2010).
[73]R. S. McWilliams, J. H. Eggert, D. G. Hicks, D. K. Bradley, P. M. Celliers, D. K. Spaulding, T. R. Boehly, G. W. Collins, and R. Jeanloz, Phys. Rev. B **81**, 014111 (2010).
[74]R. Perriot, Y. Lin, V. V. Zhakovsky, N. Pineau, J. H. Los, J.-B. Maillet, L. Soulard, C. T. White, and I. Oleynik, in *Shock Compression of Condensed Matter—2011*, edited by M. L. Elert, W. T. Buttler, J. P. Borg, J. L. Jordan, and T. J. Vogler (AIP, Melville, NY, 2011), p. 1175.
[75]D. G. Pettifor and I. I. Oleinik, Phys. Rev. B **59**, 8487 (1999).
[76]I. I. Oleinik and D. G. Pettifor, Phys. Rev. B **59**, 8500 (1999).
[77]D. G. Pettifor and I. I. Oleinik, Phys. Rev. Lett. **84**, 4124 (2000).
[78]D. G. Pettifor and I. I. Oleinik, Phys. Rev. B **65**, 172103 (2002).
[79]D. G. Pettifor and I. I. Oleynik, Prog. Mater. Sci. **49**, 285 (2004).
[80]S. J. Plimpton, J. Comput. Phys. **117**, 1 (1995); http://lammps.sandia.gov.
[81]The SED-REBO and SED-REBO-S modules implemented in LAMMPS can be obtained from the authors by sending a request to oleynik@usf.edu.